Robust quantitative X-ray phase diagnostic for carbon composite characterisation in the context of lightning induced risk

Laureen Guitard, Adrien Stolidi, Georges Giakoumakis, Rafael Sousa Martins, Jérôme Primot, Amelie Jarnac

scientific reports

Check for updates

OPEN

Robust quantitative X-ray phase diagnostic for carbon composite characterisation in the context of lightning induced risk

Laureen Guitard[1,2], Adrien Stolidi[1], Georges Giakoumakis[1,2], Rafael Sousa Martins[3], Jérôme Primot[2] & Amelie Jarnac[3]✉

Getting complementary physical information from a single image acquisition is particularly valuable for materials analysis. Grating based X-ray Phase Contrast Imaging (XPCI) methods allow decoupling attenuation, phase and scattering information. However, the phase and scattering extraction processes can easily suffer from artefacts, which is detrimental to implement this imaging technique in societal applications. In this paper, we demonstrate that grating based XPCI can provide a robust phase measurement in complex materials such as damaged composites. The technique allows the phase to be analysed using a self-assessment method that first identifies the artefacts from the imaging setup, and then can be used as an indicator to interpret the signal from a material. We focus on carbon fibre reinforced polymers which we subjected to laboratory-controlled lightning strikes. We evidence that the combined information from phase and attenuation allow identifying the type of defect induced by the lightning current. The phase information is converted into relative mass density variation within the sample and depicts areas with a loss in density up to 40%. We ensure that these results are valid by comparing them with an X-ray attenuation contrast tomographic reconstruction.

Composites materials, particularly carbon fibre reinforced polymers (CFRP), are increasingly being used in the aerospace industry for their strength and lightness, as part of the drive towards sustainable aviation. By construction, CFRP is a multi-layered composite, embeded in an epoxy matrix, made of successive unidirectional layers oriented in different directions with each layer made of aligned carbon fibres. As a result, contrary to traditionally used aluminium, CFRP has low and anistropic thermal and electrical conductivities[1]. When CFRP materials are struck by lightning, these properties reduce the efficiency of the lightning current dissipation. The current is forced to circulate along the fibres, confining the thermal effects within the layers. This alters the matrix by melting, sublimation or evaporation leading to fibre detachment. The trapped hot gases cause internal defects such as delamination, fibre breakage and puncture[2–4].

In order to take appropriate action and protect composites from lightning damage[5], it is essential to characterise the physical properties of damaged CFRP to quantify the nature and what constitutes the damage in order to recalibrate numerical damage models. In the interest of preserving the sample, numerous Non-Destructive Testing (NDT) approaches are explored. Some of these methods, such as ultrasonic[6] and acoustic emission[7], enable to get information such as sizing of cracks, flaws, delaminations and fatigue detection thanks to in-depth cross-sectional information from the CFRP. But, the anisotropic sound velocity distributions of composites result in complex wave propagation making it difficult to accurately assess the properties and location of damage[8]. Other techniques including thermography[9] and laser shearography[10] allow to evaluate debonding, fibre fluctuation and the porosity rate[11]. But these methods only allow the study of the surface or the first layers.

Among NDT techniques, X-ray imaging offers high-resolution volumetric inspection capabilities and the possibility to derive multiple information about the material such as physical (density, composition,...) and diffusive properties (porosity). X-ray Phase Contrast Imaging (XPCI) offers the possibility to measure at once the attenuation, the phase and scattering properties from which can be derived the linear attenuation coefficient μ and the refractive index decrement δ. Measuring the phase ϕ is particularly interesting since it is proportional to the material density, as per the following formulas[12]:

[1]Université Paris-Saclay, CEA, List, F-91120 Palaiseau, France. [2]DOTA, ONERA, Université Paris-Saclay, 91120 Palaiseau, France. [3]DPHY, ONERA, Université Paris-Saclay, 91120 Palaiseau, France. ✉email: amelie.jarnac@onera.fr

$$\phi = E_p \frac{2\pi\delta}{\lambda} \text{ with } \delta(\lambda) = \frac{r_e\lambda^2}{2\pi}\sum_j n_j f_j^1(\lambda) \quad (1)$$

where E_p is the thickness of the sample, λ is the wavelength, r_e is the classical electron radius, n_j and f_j^1 are respectively the atomic density and the real component of the atomic scattering factor of the j^{th} element of the material. When X-ray photon energies are away from absorption edges, f_j^1 can be approximated by Z the atomic number[13]. The term $\sum_j n_j f_j^1$ reflects the ρ_e the electronic density and Eq. (1) can be written as[13]:

$$\delta(\lambda) = \frac{r_e\lambda^2}{2\pi}\rho_e = \frac{r_e\lambda^2 N_a\rho}{2\pi}\sum_j q_j\frac{Z_j}{A_j} \quad (2)$$

where N_a is the Avogadro's number, ρ is the material density, q is the mass fraction and A is the atomic mass.

In XPCI, two primary methods can be implemented for measuring the phase shift of the wavefront. The first method, known as free propagation-based imaging, leverages the local wavefront curvature induced by phase-shifting materials [14,15]. This allows the visualization of abrupt transitions in the refractive index via the Fresnel diffraction fringes. The phase is retrieved using algorithm based on prior knowledge on the sample material or the wavefront propagation formalism[16]. To reduce the a priori sample knowledge, which leads to residual phase contrast at interfaces after the phase retrieval process, Alloo et al. recently proposed to model the attenuation parameter β using an error function [17]. This method successfully extracted accurate quantitative information on the decrement δ of the refractive index of an unknown composite sample. Nevertheless, this method has been applied on thin tomographic slices, where interfaces are sharp and still rely on the assumption that δ/β is constant, which is not the case for polychromatic laboratory-based X-ray source. Consequently, obtaining quantitative refractive index values from radiography on polychromatic X-ray source remains challenging, especially for materials with several levels of density or atomic numbers, such as the samples in this study. The second method is differential phase measurement, which employs a reference pattern, a modulator placed between the source and the detector [18–20]. When a phase object is introduced into the optical path, causing wavefront deviation, this pattern becomes distorted. The intensity pattern can be either randomly - speckle-based techniques [21,22] - or regularly - grating-based techniques [23] - distributed. In the case of speckle-based methods, the intensity pattern - often sandpaper - is achieved by attenuation contrast, which can lead to low level of contrast and difficulty tracking distortions. On the other hand, in the case of grating-based methods, the intensity pattern (or interferogram) is achieved by generating interferences using a periodic phase grid, allowing for higher contrast. The periodic pattern can be post-processed in the Fourier domain, which allows to measure the phase shift of the wavefront in several directions using only one interferogram [24]. This directional capability is particularly useful for sample with intrinsic orientation such as layered CFRP. Grating-based methods requires a spatially coherent X-ray source (source size of a few microns) to generate the interferogram with a good contrast, a phase grating and a high-resolution detector with a pixel size of a few microns to accurately sample the interferogram. Alternatively, additional gratings are needed [25]: (i) an absorption grating can be placed in front of the source to re-generate several coherent sources and/or (ii) in front of the detector to reduce physically the pixel size.

Quantitative phase measurement using multi-grating based XPCI has been validated on phantom materials (ethanol, PVC, PMMA, aluminium...), first with monochromatic[20,26] and then with polychromatic[27] or dual energy[28] X-rays, where it was shown that by exploiting phase and attenuation measurements, the density and effective Z of the material could be accurately recovered. To date, studies on damaged CFRP has focused on detecting defects, either induced intentionally (microcrack, porosity,. . .)[29–31] or induced by mechanical impacts (cracks, delamination. . .)[32]. To our knowledge, materials with undetermined physical properties have not been subjected to quantitative grating based XPCI characterisation.

In this paper, we characterize damages on non-conventional materials, specifically lightning-struck CFRPs, which exhibit heterogeneous composition and unknown stoichiometry post-lightning strike. Taking advantage of a spatially coherent X-ray source and a high resolution detector, we performed XPCI using a single phase grating technique termed as Multi Lateral Shearing Interferometer (MLSI)[33–35]. In the studied case, the MLSI offers the possibility of adjusting the interferogram period to sample phase variations more easily than multiple grating setups. To provide quantitative and robust characterization, we calibrated the imaging setup using a standard sample and validated the imaging condition for CFRP by putting in place a self-assessment method based on the closure of the phase derivative which allows to detect artefacts in the phase reconstructed image. We imaged pristine and lightning damaged CFRPs and filtered and reconstructed the phase according to the CFRP fibre directions. A first qualitative analysis reveals complementary information between phase and attenuation about the lightning induced damages. Subsequently, we converted the phase information into relative density variation of lightning-struck CFRP. Finally, we confirm the localization and extent of damages in the CFRP samples through a classical attenuation contrast X-ray tomography.

Results and discussion

Lightning-damaged CFRP coupon

The studied sample are two coupons made of CFRP with one being subjected to controlled lightning conditions on a lightning bench. To inject lightning current into the core of the CFRP, it is necessary to drill holes and insert one screw as an entry point and another as an exit point. Then the current distribution path is imposed by an atypical multilayered arrangement (+45°, -45°), instead of the one used in the industry (+45°, +90°, -45°, 0°). This arrangement theoretically ensures that all plies contribute equally to current transport within the CFRP and gives two privileged directions. The sample was submitted to representative levels of current experienced

by aircraft in operation. Indeed, when an aircraft is struck by lightning, the current flows along the fuselage and is distributed among the structural fasteners (screws) near the point of lightning entry. As a result, a fastener experiences a fraction of the maximum lightning current, which can be as high as 200 kA. To ensure that the CRFP was damaged, we gradually increased the lightning current slightly over the sparking occurrence (which results from the bad electrical contacts between the CFRP and the screw). Sparking occurred at 18 kA, and we shot three more times at 24, 29 and 36 kA. More details are reported in the Methods section.

Phase gradient revealed by MLSI based XPCI

To characterise the CFRP coupons, we implemented the MLSI method[33–35] as grating based XPCI method. The method's schematic is depicted in Fig. 1. This approach requires a single 2D phase grid (checkerboard pattern) in the optical path to generate the interferogram. To efficiently generate and sample the interferogram, the setup requires a X-ray source with a micrometer spot size and high-resolution detector. With this setup, we first image the grid alone to obtain the reference interferogram. The sample is then brought into the field of view and a new image is acquired. The interferogram on the detector is altered by the introduction of the sample. We analyse this modified interferogram in the Fourier domain according to the process outlined in Fig. 2. In the Fourier domain, the periodicity of the grid implies the presence of harmonics $H_{k,l}$ along eight principal directions $\vec{w} = k\vec{x} + l\vec{y}$ with $k, l \in \{0; \pm 1; \pm 2\}$. The harmonics correspond to spatial frequencies along these directions. To retrieve

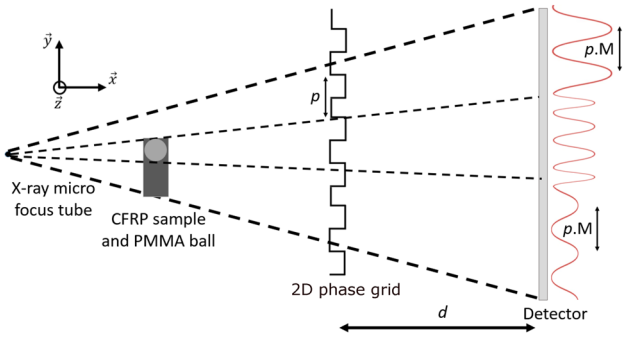

Fig. 1. Diagram of the laboratory setup using the MLSI method composed of a divergent micro-focus tube with a magnification M, a single 2D phase grid p-periodic and a high-resolution detector.

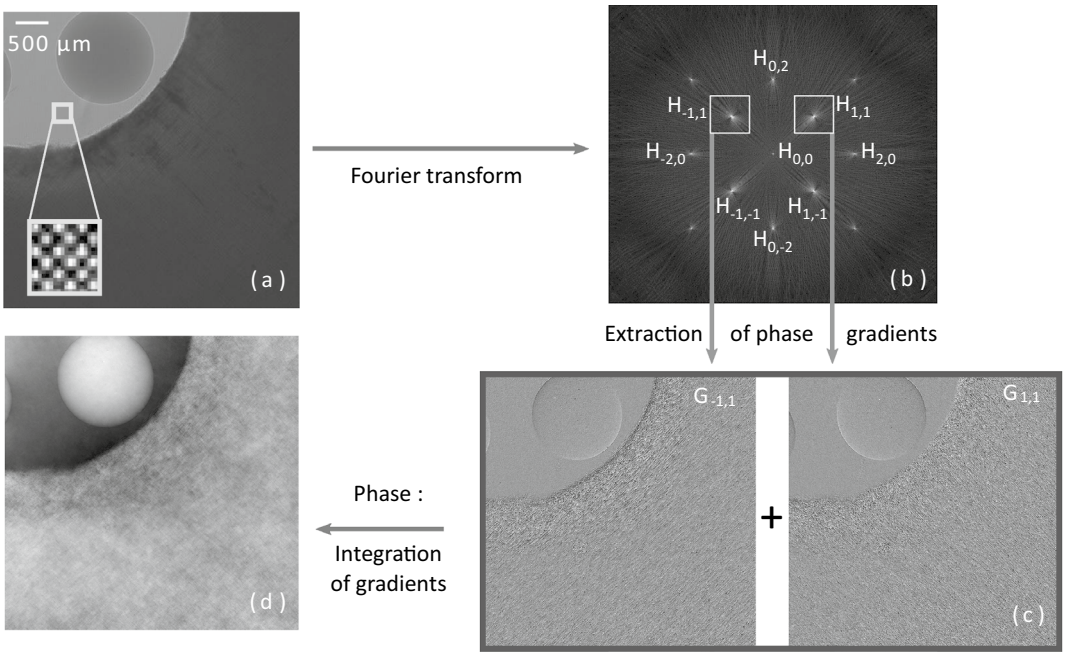

Fig. 2. Explanatory diagram of the gradient extraction method in the Fourier domain and phase retrieval. (**a**) Image of the damage CFRP and the PMMA sphere with the grid in the (y,z) plane. (**b**) Fourier transform of the image, corrected from the $H_{0,0}$ contribution[36]. (**c**) Phase gradients $G_{-1,1}$ and $G_{1,1}$ retrieved from $H_{-1,1}$ and $H_{1,1}$ respectively [24]. (**d**) Phase retrieved from the gradients.

the phase gradient $G_{k,l}$, it is necessary to compute the argument of the inverse Fourier transform of $H_{k,l}$ over a window of extraction centred on the carrier frequency[24] :

$$G_{k,l}(x,y) = \frac{p}{2\pi d} \cdot \arg\left(\mathscr{F}^{-1}\left[H_{k,l}(u,v)\right]\right) \tag{3}$$

With (x, y) representing the coordinates in real space and (u, v) their associated coordinates in reciprocal space, $\mathscr{F}$ denotes the Fourier transform, p is the periodicity of the grid and d is the propagation distance between the grid and the detector. The phase $\phi(x, y)$ is then derived from two orthogonal gradients using the Fourier derivative theorem :

$$\phi(x,y) = \mathscr{F}^{-1}\left[\frac{\mathscr{F}\left(G_{k,l} + iG_{-l,k}\right)}{2i\pi(u+iv)}\right] \tag{4}$$

Since the CFRP contains high accutance details such as the fibres or edges, the harmonic $H_{0,0}$ (depicted in the Fig. 2) that carries attenuation information and edge intensity overshoot (linked to the laplacian phase) is extended in the Fourier domain. This extension overlaps with the grating harmonics $H_{k,l}$ resulting in artefacts during phase reconstruction[36]. To reduce the occurrence of artefacts, we used the method proposed in Ref.[36], which requires acquiring an additional image of the sample without the grid, including a fully fluxed area.

The image acquired in the presence of the grid for the damage CFRP sample is shown in Fig. 2a. Since the multilayered arrangement of the CFRP is along (+45°,-45°), we select the harmonics $H_{x,y}$ and $H_{-x,y}$ ($H_{1,1}$ and $H_{-1,1}$ in Fig. 2b) to retrieve the phase gradient as observed in Fig. 2b,c. Using these gradients, we integrate and obtain the phase $\phi(x, y)$ shown in Fig. 2d.

Robustness of the phase retrieval

Despite the efforts made to reduce the occurrence of artefacts, the reconstructed phase can still be affected by different errors, such as dislocations due to abrupt phase variation from 0 to 2π radians, undersampling due to sharp phase variation, and noise. These errors can be detected by a self-assessment method using the Confidence Map[37]. This method uses the closure of the phase derivative which is a system based on phase gradient measurement. When there is no reconstruction error, the closure of the phase derivatives $C(x, y)$, which is calculated with

$$C(x,y) = \partial_{x,y}\, G_{-x,y} - \partial_{-x,y}\, G_{x,y} \tag{5}$$

equals to zero. But in the case of errors, each of them contributes to $C(x, y)$ in the form of $C(x, y) = \varepsilon_u + \varepsilon_d + \varepsilon_n$. The Confidence Map is a method used to categorize each error contributions, including under sampling (ε_u), dislocations (ε_d), and measurement noise (ε_n). If the dislocation and undersampling contributions depend solely on the sample being imaged, the noise depends on the photon noise, which is a combination of the X-ray source, the sample attenuation, and also the detector electronic noise.

Another source of inaccuracy when evaluating the absolute value of the phase is the influence of the polychromatic spectrum of the X-ray tube. To address this issue, we quantitatively calibrate the setup using a standard. Each sample image contains a sphere made of polymethyl methacrylate (PMMA) from Goodfellow with a diameter of 1.5 ± 0.05 mm and a density of 1.19 g/cm^3 (manufacturer data), which exhibits a phase of 142 radians at the average energy of the spectrum (10 keV). The sphere also serves as a reference standard to ensure on each image favorable conditions for comparing different measurements, using the self-assessment method. Since we study one kind of material (CFRP), the noise depends only on the imaging system and does not provide any information on material damage.

Given that the noise contribution is homogeneous and similar across the images (see Fig. 10b), we focus on the contributions arising from dislocation and under sampling errors. These values can be studied on the pristine sample of CFRP and the PMMA sphere. In the Fig. 3, a Region of Interest (ROI) of 195×195 pixels is selected in the PMMA sphere and one of 525×525 in the pristine CFRP. For each of these ROIs, the percentage of dislocation and under sampling alerts is calculated. This means that we observe the number of pixels that light up as an indication of dislocation or under sampling within the ROI, divided by the total number of pixels of the ROI. The PMMA sphere shows 0.08% dislocation alerts and 0.03% under sampling alerts. These values will serve as a reference later on. On the other hand, the CFRP sample, shows about 0.53% dislocations and 0.30% under sampling. Despite being a complex object compared to the PMMA sphere, the number of alerts for the pristine CFRP is low, indicating that the imaging system provides proper analysis conditions and that the homogeneous distribution of fibres in the pristine sample allows for good sampling.

Attenuation and phase contrast information

In order to increase the field of view of the detector while maintaining high resolution, we perform a stitching to combine multiple phase measurements of the sample into a global image. The Fig. 4 depicts the stitching of the lightning-struck sample in attenuation (a) and in phase (b) contrast. On each image of the stitching, we place a PMMA sphere next to the CFRP to control the calibration and the imaging conditions. The PMMA sphere cannot be seen in Fig. 4a because the contrast dynamic is adjusted to the CFRP.

The attenuation contrast image exhibits highly absorbent features, particularly in the lower right corner of the hole. It is worth noting that these features are neither present in the phase image nor in the form of edges in the gradient images (shown in Fig. 2c). We recall here that the attenuation contrast depends on the linear attenuation coefficient μ and the phase contrast depends on the refractive index decrement δ. Let's consider that the CFRP is

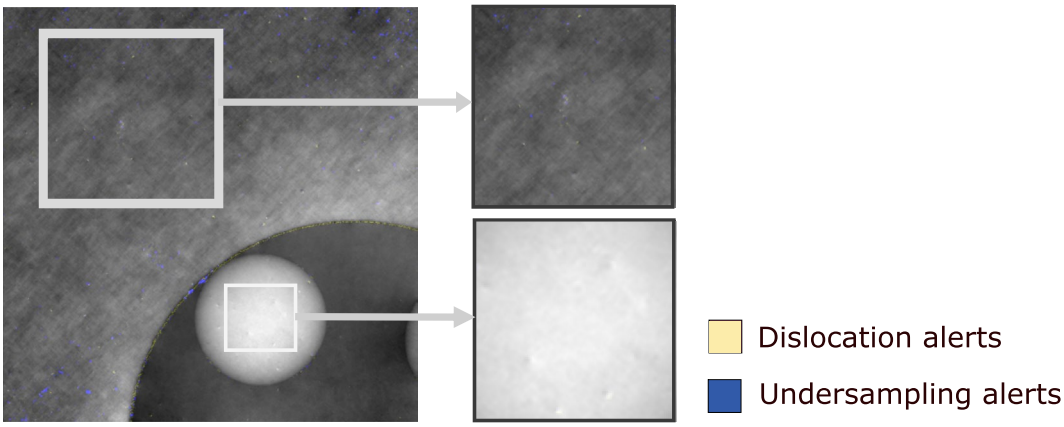

	ε_d	ε_u
ROI in PMMA	0.08%	0.03%
ROI in Pristine CFRP	0.53%	0.30%

Fig. 3. Implementation of a self-assessment method based on the confidence map[37] on a phase image of a PMMA standard sphere and a pristine CFRP sample. The undersampling alerts (ε_u) are shown in cyan and the dislocation alerts (ε_d) are in yellow. The statistical analysis is performed on ROI of 195×195 pixels for the PMMA standard sphere and on 525×525 pixels for the pristine CFRP. The results are reported in the table, indicating the percentage of dislocation and undersampling values for the two ROIs.

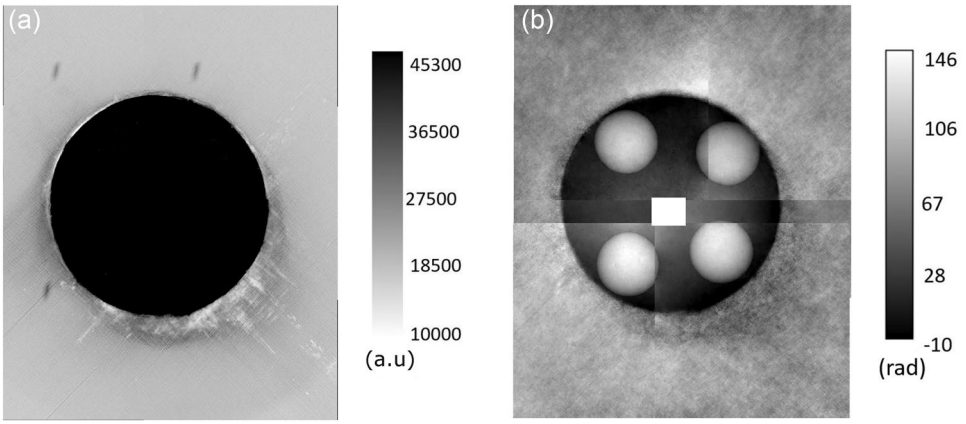

Fig. 4. Stitching of the lightning damage CFRP coupon. (**a**) Attenuation contrast image. Note that the darker the contrast, the lighter the material. The contrast dynamic is adjusted to the CFRP so the PMMA sphere cannot be seen. (**b**) Extracted phase contrast image. The imaged area can be seen as the red square in the Fig. 9.

primarily composed of carbon. At the average energy of the spectrum of 10 keV, μ is governed by the electronic cross-section for photoelectric absorption σ^e_{ph}, and can be approximated as $\mu = \rho_e \sigma^e_{ph} = \rho_e \times const. \frac{Z_{eff}}{E}$[13,38], Z_{eff} is the effective atomic number of the material and E the X-ray energy. On the other hand, δ is solely governed by ρ_e (Eq. 2). By exhibiting no phase signal these features correspond to a damage with low ρ_e, but by exhibiting attenuation signal it indicates a damage with high Z_{eff}. As demonstrated in[27], compounds such as polymers can have similar electronic density but very different Z_{eff} ($\rho_{e,PMMA} = 3.87 \cdot 10^{29}$ m^{-3} and $Z_{eff,PMMA} \approx 6$, but $\rho_{e,PVC} = 4.32 \cdot 10^{29}$ m^{-3} and $Z_{eff,PVC} \approx 14$). Therefore, we can reasonably assume that this post-lightning damage corresponds to the resin that has changed composition and contains heavy atoms (i.e C or Ti) as indicated by an increased Z_{eff} while maintaining its initial density.

To further interpret the phase information, we apply the self-assessment method based on the Confidence Map results on the PMMA and CFRP ROIs defined for each image of the stitching (ROIs are reported on Fig. 11 in "Methods" section). The results are shown in Table 1. The alert values of the PMMA spheres are similar to those in Fig. 3, validating the measurement comparisons. However, the dislocation and under sampling alerts are higher in the damaged CFRP than the pristine sample ($\varepsilon_d = 0.53\%$ and $\varepsilon_u = 0.30\%$). In particular, the area (d) experiences 5.91% dislocations alerts and 30.36% under sampling alerts. Moreover, the phase image (Fig. 4b bottom right) displays a low contrast area, suggesting presence of an intrinsic defect in the sample. From the

		ε_d (%)	ε_u (%)
a	PMMA	0.03	0.02
	CFRP	0.53	2.07
b	PMMA	0.08	0.00
	CFRP	1.05	5.18
c	PMMA	0.02	0.03
	CFRP	1.89	10.52
d	PMMA	0.06	0.03
	CFRP	5.91	30.36
e	PMMA	0.03	0.00
	CFRP	1.64	7.00
f	PMMA	0.03	0.01
	CFRP	2.63	12.34

Table 1. Values of dislocation ε_d and undersampling ε_u alerts of the lightning damaged CFRP and PMMA spheres derived from the confidence map from respectively 525×525 and 195×195 pixels ROI.

number of under sampling alerts, we can assume that, even if the defect is macroscopic, what constitutes the defect is smaller than the fibres, and that the fibre constitution is no longer homogeneous through the CFRP and thus not well sampled by the interferogram. Furthermore, the defect is oriented at -45°, which is similar to the orientation of 50% fibres. This suggests that the defect is due to the current that has flowed along the fibres and degraded the sample along its path. It was anticipated that the current would be evenly distributed between both fibre orientations at +45° and -45°, but it appears that one orientation was favoured.

It should be noted that despite the efforts made to guarantee the information provided by the phase extraction and the calibration, the absolute phase value obtained in the CFRP should be interpreted with caution. Indeed, in first approximation, the phase value of a 4 mm thick CFRP should be approximately twice that of the PMMA standard sphere, assuming as principal compound carbon and a density of around 1.5 g/cm^3[1]. This is not the case in Fig. 4b, which can be explained by phase wraps occurring during the wave propagation in the non-homogeneous CFRP, which induces a sharp thickness variation from 0 to 4 mm. This phenomenon does not occur in the PMMA sphere since its thickness variation evolves continuously.

Density variation

It is of interest to pursue a quantitative approach. To overcome phase wrapping and quantify the damage in terms of the CFRP density, a preliminary approach is to provide a quantitative variation of density across the damaged area. To do so, we examine an undamaged region (top of the sample, yellow square on Fig. 9) and obtain its average pristine phase value ϕ_0. We then calculate the density variation as:

$$\Delta\rho(x,y) = \Delta\phi(x,y) = \frac{\phi(x,y) - \phi_0}{\phi_0} \tag{6}$$

assuming that the proportions of various atomic elements have not changed. These results are reported in Fig. 5a as a color map of the percentage density variations. The color bar is centred in zero, meaning that white areas correspond to regions where the density remains unchanged; purple areas correspond to regions where the density is lower than the initial density; and green areas correspond to regions where the density is higher than the initial density.

To determine the uncertainty of this evaluation, we perform the same procedure on the pristine sample. The resulting relative density variation is shown in Fig. 5b. It can be observed that 99% of the density variation distribution amounts to ± 21.9% (3σ). On the other hand, the lightning damaged CFRP exhibits a purple zone at the lower right edge of the hole, indicating a reduction in density of approximately 40%. Two green areas are visible : the first one located at the top right of the hole, depicts an increase in density of 60% ; the second one located at the bottom left of the sample, depicts an increase in density of 20% but it may not be entirely reliable as it is too close to the sensitivity of the measurement.

Method validation by comparison with tomography

The results presented so far arise from a 2D radiography in which the information is integrated over the entire thickness. To validate our findings and interpretations, we compare the attenuation and phase measurement to another well-known non-destructive testing tool using X-rays, attenuation contrast tomography. Tomography reconstruction allows for good contrast despite low attenuation thanks to a large amount of projections. From the tomogram, we obtain a detailed three-dimensional reconstruction of the lightning damaged CFRP. This 3D volume, allows to extract slices from the inner part of the sample.

Figure 6 presents three selected slices : (a) and (b) in the $(\mathbf{y}, \mathbf{z})$ plane and (c) in the $(\mathbf{x}, \mathbf{z})$ plane. In Fig. 6a a low density trench is visible in the lower right corner of the hole. In addition, Fig. 6b shows a low density halo at the bottom edge of the hole and Fig. 6c shows that this halo extends through the entire thickness of the sample. From the tomogram, we can determine the in-depth extent of the trench and the halo. The trench is about 425 µm,

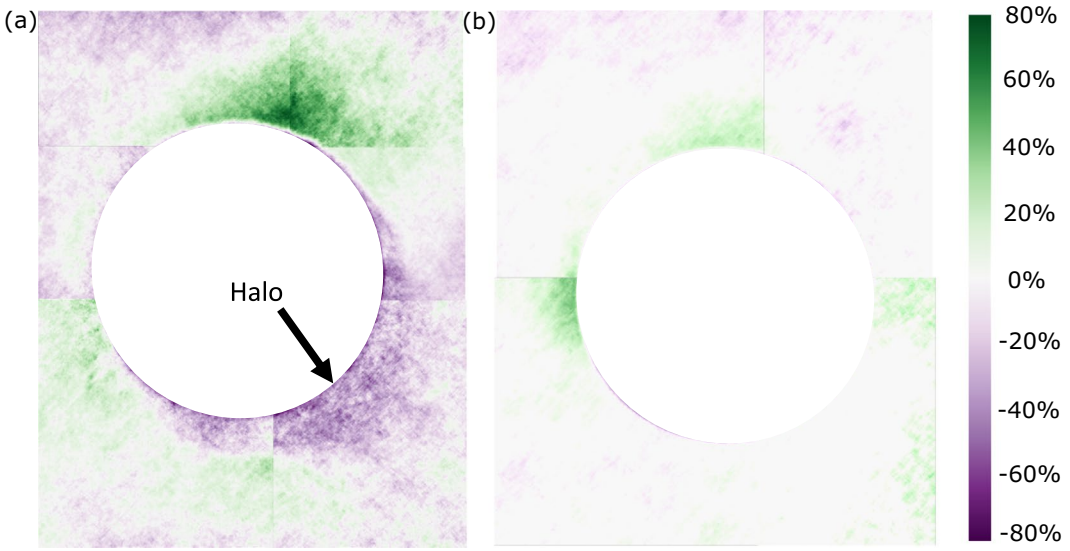

Fig. 5. Color map of relative density variation of (**a**) the lightning damaged CFRP and (**b**) the pristine CFRP.

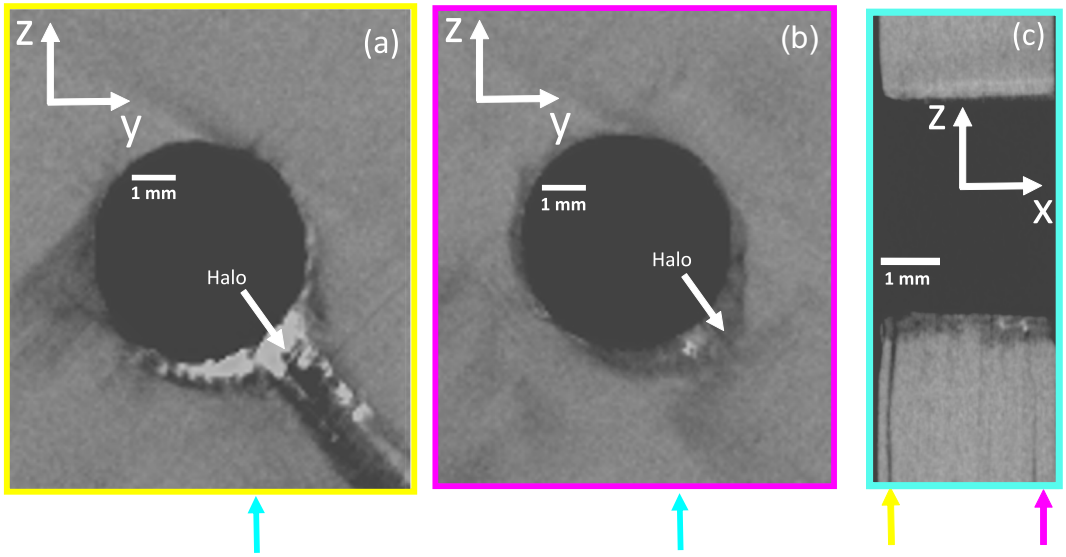

Fig. 6. Reconstructed slices of the lightning damaged CFRP. (**a,b**) Slices in the (**y**, **z**) plane respectively at x = 275 µm and 3.8 mm from the front of the sample and (**c**) show a slice in the (**x**, **z**) plane at y = 2.4 mm from the left edge of the sample. In these images, the darker the contrast, the lighter the material.

which represents 10.36% of the thickness. This proportion is smaller than the density variation sensitivity. However, the halo represents 46.45% of the thickness which is in good agreement with what is observed in Fig. 5.

In Fig. 6c, a more absorbent area appears at the top edge of the hole over the thickness. The change in contrast does not seem to corroborate the 60% increase of density seen in Fig. 5. It is possible that the assumption of unchanged proportions of atomic elements does not hold here. Indeed, a change in proportion or in elements would contribute to a phase change (see Eq. 1). An increase in phase contrast could arise from a permanent doping of metallic ions from the current infection screw. Indeed, it can be seen in the Fig. 8b that the studied area (fastener 1) has been subjected to sparking phenomena. During this phenomena, the shank of the screw undergoes melting and vaporization and the surrounding materials undergo a strong overpressure [39]. Moreover, the current was injected through this fastener, meaning that the CFRP emitted electrons and the screw emitted positive metallic ions. The internal pressure and electric field combined together could have favored the diffusion and implementation of metallic ions in the CFRP in the vicinity of the current injection area. Also, notice that the tomography reconstruction is not calibrated. Therefore the gray level dynamic, which is related to the experimental conditions (spectrum, noise) and the reconstruction algorithm (type of filtration), cannot be quantitatively compare to the Fig. 5.

Conclusion

To conclude, we investigated the potential of the grating based XPCI technique to characterise materials with undetermined physical properties. We focused on CFRPs, which are increasingly used in aeronautic industry. In particular, we examined CFRPs damaged by lightning, which lacks a quantitative characterisation of their post-lightning physical properties. This lack of data prevents from recalibrating numerical damage models. The proposed XPCI approach based on MLSI highlights some advantages for the CFRP characterisation: (i) decoupling attenuation and phase with a spatial resolution down to 5 µm (depending on the bench parameters); (ii) spatial filtering, linear and quantitative phase extraction treatments thanks to the Fourier analysis and (iii) self-assessment of the errors. In the context of lightning induced damage, these advantages offer the possibility to be sensitive to damage to the fibers, to discern the type of defect and its direction. We also evidenced that the phase in addition to attenuation information help to identify the nature of the damage. The self-assessment method, which use the Confidence Map method, an intrinsic information derived from the grating based reconstruction procedure, is a valuable tool for interpreting the signal. First, it ensures that the imaging conditions are optimised and that errors in the phase reconstruction are avoided. Then, when characterising an unknown material, the number of alerts indicates where is the signal to interpret, how to interpret it and possibly, how to tweak the imaging system to better image this specific area. For instance, increase the sampling in the case of under sampling alerts. We developed a quantitative approach to analyse the relative phase variation. This evidenced areas with loss or gain in density induced by the lightning current circulation in the CFRP. These observations have been confirmed by an X-ray attenuation tomography of the damage CFRP. It is interesting to note that in the 2D phase image, which is integrated over the thickness, we retrieve features only observed thanks to slices extracted from the 3D tomographic reconstructed volume. However, the sensitivity threshold of about 20% in the density variation prevents from detecting thin defects (here < 0.8 mm). A parametric study on a larger amount of samples should improve the sensitivity of the density variation.

Eventually, MLSI method is a promising high-resolution X-ray phase imaging method that offers significant advantages in terms of robustness, throughput, sensitivity to fibre orientation, resolution, and compactness for studying complex and innovative composite materials. This laboratory setup also enhances accessibility to phase-contrast X-ray imaging and is currently advancing towards the development of quantitative phase tomography capabilities.

Methods

Lightning setup and sample description

The current generator used in this work is the ONERA's lightning test facility, named GRIFON. This generator is built in an approximated RLC circuit and is able to deliver a transient component of the standard current waveform as defined in aeronautical recommendation documents[40]. Aiming to perform a complete characterization of CFRP damage across a wide range of current levels, the generator has been adapted to deliver fractions of the transient D-component, with waveforms of the same shape ranging from 10 A to 36,000 A peak. Figure 7 presents some of these waveforms, which are applied to the CFRP sample. For more details about the GRIFON generator, interested readers are referred to Ref.[41].

The sample subjected to the lightning waveform is made using a CFRP coupon as the external structure (the skin) and two aluminum plates as the inner structure (the rib). To keep the specimen as simple as possible, only two fasteners are used in the CFRP, each one assembling the skin to one rib. The current is injected into the aluminum rib 1 and collected by the aluminum rib 2 as depicted in the diagram in Fig. 8a. A dielectric sheet (NOMEX T410 with a thickness of 250 µm) is inserted between the parts for insulation, ensuring that the

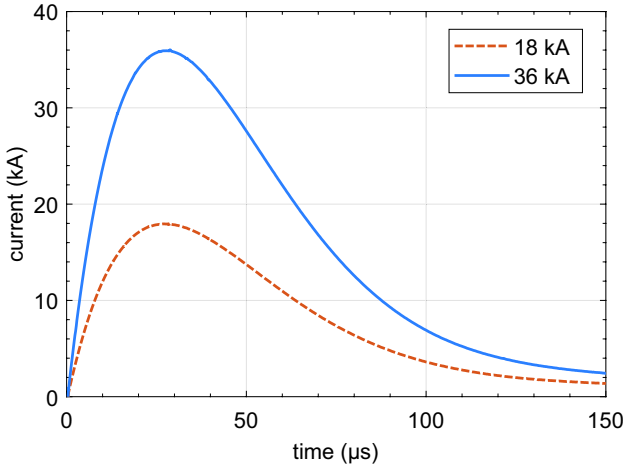

Fig. 7. Selection of transient current waveforms applied to the CFRP coupon. The waveforms are based on a D-component of aeronautical recommendation standards. The maximum current reached by the waveform is reported in the caption. The sample experienced sparking at 18 kA and was shot three more times at 24, 29 and 36 kA.

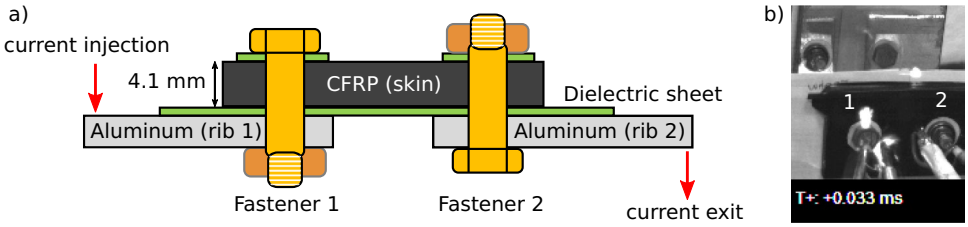

Fig. 8. (**a**) Diagram of the sample subjected to the lightning current, including a CFRP coupon and two aluminum plates. The sample is kept simple to control the circulation of current in the CFRP and locate the current injection and exit points. (**b**) Frame of the high-speed video monitoring the lightning test extracted at a delay of 33 µs after the current injection. The area of Fastener 1 undergoes damage as evidenced by the sparking phenomena.

Fig. 9. Photo of the CFRP coupon struck at the ONERA's lightning test facility with the GRIFON generator. The red square corresponds to the area of fastener 1 and is the imaged zone on the CEA's MSLI-XPCI installation. The yellow square corresponds to the undamaged region used to measure the average pristine phase value ϕ_0.

current can only flow from the fastener 1 to the fastener 2, through the skin. During the current injection, the sample was monitored by a high-speed camera. Figure 8b shows the frame taken at a delay of 33 µs after the beginning of the current injection. One can see that fastener 1 undergoes sparking. After the lightning test, the CFRP coupon is unmounted to image this area on the CEA's MLSI-XPCI bench. A photo of the CFRP coupon after lightning test is shown in Fig. 9.

The CFRP coupon is composed of 16 unidirectional pre-impregnated carbon reinforced epoxy plies, each one made of T700 carbon fibers (Toray) inside a thermosetting resin of epoxy M21 (Hexcel). The layup structure is made with ply orientations at 45° and −45°, creating an atypical layup where there is no privileged ply to carry current between the two fasteners. The CFRP coupon has dimensions of 50 × 30 × 4.1 mm sideways.

Multi-lateral shearing interferometer installation

We have developed a laboratory bench using a single grating. The system consists of a polychromatic micro-focus tube, an interference grid, and a detector (Fig. 1). We use a Hamamatsu microfocus tube with a tungsten anode, a voltage of 60 kV and a current of 35 µA. The measured focal spot size is 8 µm. A grid from MicroWorks company is used as a reference. It modulates the intensity of the wavefront with a phase shift of $[0\,;\pi]$ at 17.48 keV induced by a gold layer of 3.49 µm thickness deposited on a polymer substrate. A set of grids is available with different values of periodicity in order to increase the sensitivity of the measured phase of the sample. We used the grid with a periodicity p of 20 µm, positioned at a distance of 22 cm from the X-ray source. We place the lightning-struck sample in front of the grid, at a distance of 14.5 cm from the source. The installation requires a high-resolution detector to adequately sample the grid and the phase gradients. The detector is a Hamamatsu sCMOS with a 20 µm thick GadOx scintillator, 2048 × 2048 pixels and a pixel size $S_{pix} = 6.5\,\mu$m. The detector is located at a distance of 47 cm from the tube. Since the X-ray source is divergent, the setup leads to a magnification of the grid (M_g) of 2.14 and of the sample (M_s) of 3.24. The acquisition procedure is as follow: we acquire an image of the sample without the grid, an image of the sample with the grid and an image of the grid alone. In

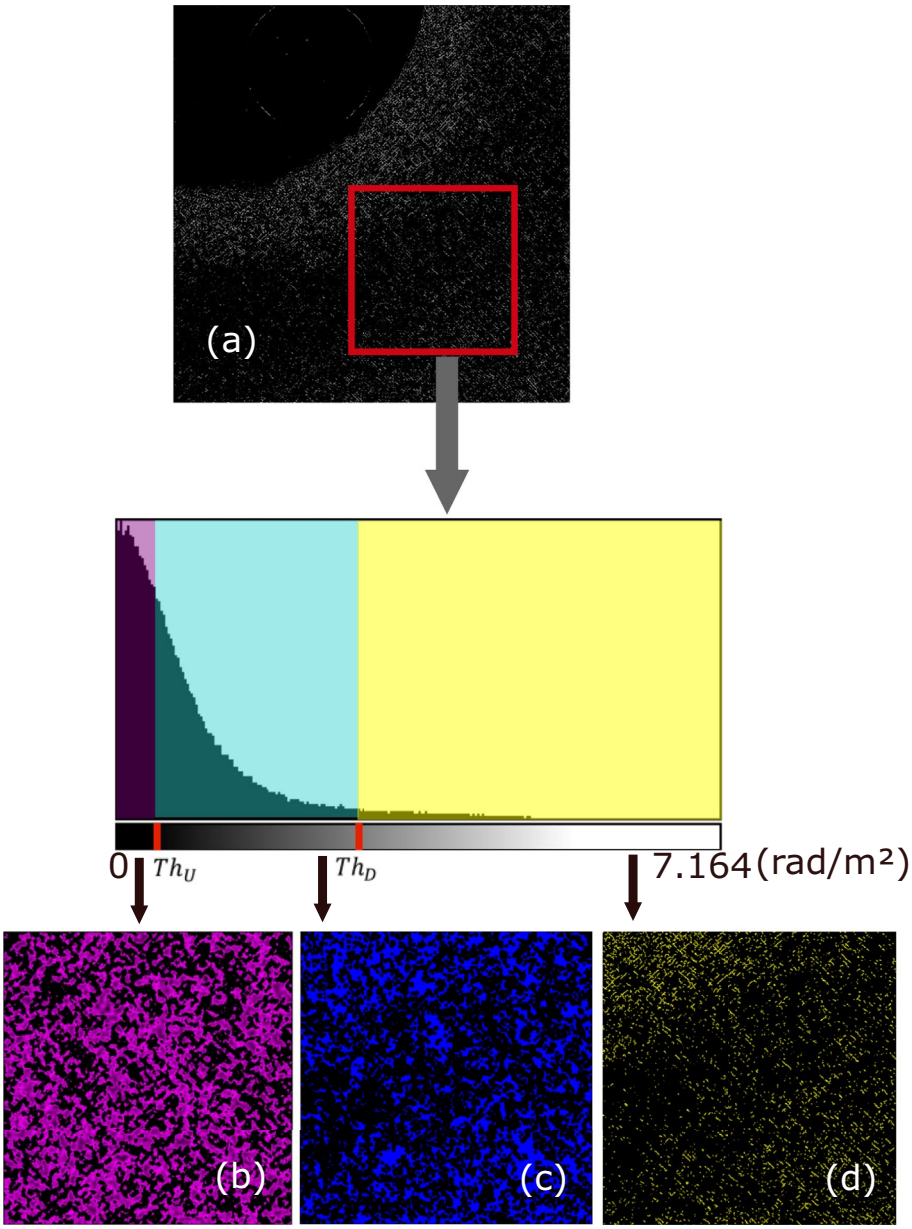

Fig. 10. Construction of the confidence map: from the phase derivative closure map $C(x, y)$ (**a**) threshold methods are applied to highlight the contribution of noise (**b**), under sampling (**c**) and the phase dislocation (**d**).

each case, we average four images taken with a 20 s exposure time. The detector response is previously corrected by a dark image and a flat field.

Construction of confidence map

Using the gradient images shown in Fig. 2 and applying the Eq. (5), we can generate the closure phase derivatives image $C(x, y)$ presented as absolute values in Fig. 10a and its associated grey values histogram. As described in[37], a confidence map can be built from this histogram. First the threshold Th_d related to the alert ε_d is calculated by using a maximum entropy method[42]. This threshold method consists of assessing the likelihood of an event occurring, in our case phase dislocation and undersampling. Here we find Th_d =2.721 rad/m^2. Then each pixel of the image $C(x, y)$ is evaluated and an alert is triggered by coloring pixel in yellow when the pixel value (x_i, y_j) exceeds Th_d. After filtering ε_d, under sampling alerts ε_u and noise alerts ε_n are calculated by evaluating the $C(x, y)$ image with a moving average evaluation window of size of $S_\Omega = (pM_g)/(2S_{pix}) = 2$ pixels in the region of interest defined by the red square in Fig. 11. To differentiate the contribution of ε_u from ε_n, we also use the maximum entropy method. The resulting threshold value is $Th_u = 0.658$ rad/m^2. All the ε_d, ε_u and ε_n are displayed in Fig. 10b–d. These images can be merged with the phase image as illustrated in Fig. 3.

The Fig. 11 displays the regions of interest (ROI) selected for applying the Confidence Map from the Table 1. The high acutance area such as the CFRP edges have been removed to not introduce irrelevant alters values.

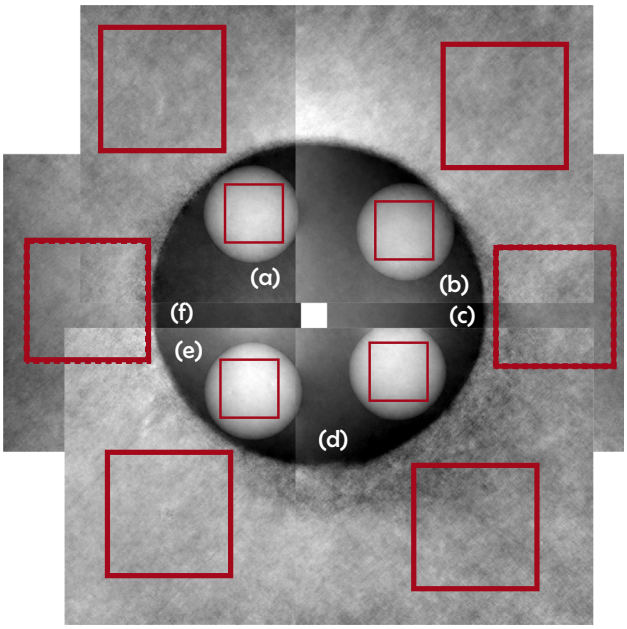

Fig. 11. Region of interest used to apply the Confidence Map. The statistical analysis is performed on ROI of 195×195 pixels for the PMMA standard sphere and on 525 × 525 pixels for the CFRP. The squares with partially dotted outlines indicate the ROIs taken in the images presented at the rear of the stitching.

X-ray tomography set-up

X-ray attenuation tomography is a non-destructive technique that enables the reconstruction of cross-sectional images of a three-dimensional object. Classical tomographic acquisition involves rotating the sample over 360° and record a 2D radiography (or projection) for each angular steps. The tomogram acquired here consists of 900 projections with an angular increment of 0.4°. The X-ray equipment are compose of a Viscom 225 kV microfocus tube with a tungsten target and a Perkin Elmer flat panel detector with 1024 × 1024 pixels of size of 200 µm. The X-ray tube voltage and current was set at 60 kV and 200 µA for an exposure time of 1 s per projection. The source-sample distance was 119 cm for a sample magnification of 4.04. The magnification was chosen to image the entire sample ($50 \times 30 \times 4$ mm^3) in order to minimize the reconstruction artefacts. As a result, the effective voxel size is 49.5 µm, which is 7 times larger than the pixel size of the XPCI measurement. But note that the observed damages are about half a millimetre in size, which is about 10 times larger than the effective voxel size. We then analyse a ROI of the same size as the phase extraction. Using these data, a digital volume image is reconstructed with Feldkamp Davis Kress (FDK) algorithm[43] and display in grey scale levels slices in Fig. 6. This method allows for a high-resolution 3D analysis of the sample. It enables to target the depth of the defect accurately.

The figure 12 shows the different directions of sections that can be obtained: in red in the $(\mathbf{y}, \mathbf{z})$ plane, in green in the $(\mathbf{x}, \mathbf{z})$ plane, and in blue in the $(\mathbf{x}, \mathbf{y})$ plane.

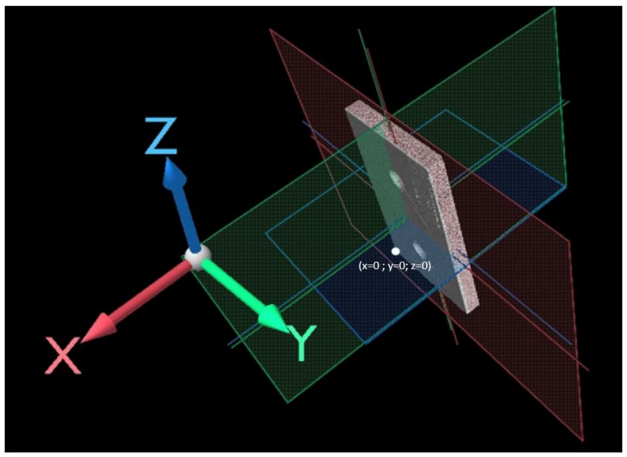

Fig. 12. Tomographic section plans used to extract the slices shown in Fig. 6.

Data availability

The data presented in this study are available from the corresponding author on reasonable request.

Received: 26 June 2024; Accepted: 3 September 2024
Published online: 18 September 2024

References

1. Chawla, K. K. *Composite Materials* 3rd edn. (Springer, 2012).
2. Chemartin, L. *et al.* Direct effects of lightning on aircraft structure: Analysis of the thermal, electrical and mechanical constraints. *Aerosp. Lab* **5**, 1–15 (2012) https://hal.science/hal-01184416.
3. Hirano, Y., Katsumata, S., Iwahori, Y. & Todoroki, A. Artificial lightning testing on graphite/epoxy composite laminate. *Compos. Part A Appl. Sci. Manuf.* **41**, 1461–1470. https://doi.org/10.1016/j.compositesa.2010.06.008 (2010).
4. Kumar, V. *et al.* Factors affecting direct lightning strike damage to fiber reinforced composites: A review. *Compos. Part B Eng.* **183**, 107688. https://doi.org/10.1016/j.compositesb.2019.107688 (2020).
5. Pandey, A., Upadhyay, A. K. & Shukla, K. K. Lightning strike response of composite structures: A review. *J. Met. Mater. Miner.* **31** (2021).
6. Helfen, T. B., Venkat, R. S., Rabe, U., Hirsekorn, S. & Boller, C. Characterisation of CFRP through enhanced ultrasonic testing methods. *Appl. Compos. Mater.* **19**, 913–919. https://doi.org/10.1007/s10443-012-9250-2 (2012).
7. Calabrese, L. & Proverbio, E. A review on the applications of acoustic emission technique in the study of stress corrosion cracking. *Corros. Mater. Degrad.* **2**, 1–30. https://doi.org/10.3390/cmd2010001 (2021).
8. Yang, H. *et al.* Ultrasonic detection methods for mechanical characterization and damage diagnosis of advanced composite materials: A review. *Compos. Struct.* **324**, 117554. https://doi.org/10.1016/j.compstruct.2023.117554 (2023).
9. Ciampa, F., Mahmoodi, P., Pinto, F. & Meo, M. Recent advances in active infrared thermography for non-destructive testing of aerospace components. *Sensors* **18**, 609. https://doi.org/10.3390/s18020609 (2018).
10. Gholizadeh, S. A review of non-destructive testing methods of composite materials. *Proc. Struct. Integr.* **1**, 50–57 https://doi.org/10.1016/j.prostr.2016.02.008 (2016) (XV Portugese Conference on Fracture, PCF 2016, 10–12 Feb 2016, Paco de Arcos, Portugal).
11. Mayr, G., Plank, B., Sekelja, J. & Hendorfer, G. Active thermography as a quantitative method for non-destructive evaluation of porous carbon fiber reinforced polymers. *NDT & E Int.* **44**, 537–543. https://doi.org/10.1016/j.ndteint.2011.05.012 (2011).
12. Attwood, D. *Soft X-Rays and Extreme Ultraviolet Radiation: Principles and Applications* (Cambridge University Press, 1999).
13. McCullough, E. C. Photon attenuation in computed tomography. *Med. Phys.* **2**, 307–320. https://doi.org/10.1118/1.594199 (1975).
14. Paganin, D., Mayo, S., Gureyev, T., Miller, P. & Wilkins, S. Simultaneous phase and amplitude extraction from a single defocused image of a homogenous object. *J. Microsc.* **206**, 33–40 (2002).
15. Turner, L. D. *et al.* X-ray phase imaging: Demonstration of extended conditions with homogeneous objects. *Opt. Exp.* **12**(13), 2960–2965 (2004) https://opg.optica.org/oe/abstract.cfm?URI=oe-12-13-2960.
16. Burvall, A., Lundström, U., Takman, P. A. C., Larsson, D. H. & Hertz, H. M. Phase retrieval in X-ray phase-contrast imaging suitable for tomography. *Opt. Exp.* **19**(11), 10359–10376 (2011).
17. Alloo, S. J. *et al.* Tomographic phase and attenuation extraction for a sample composed of unknown materials using X-ray propagation-based phase-contrast imaging. *Opt. Lett.* **47**(8), 1945–1948. https://doi.org/10.1364/OL.445802 (2022)
18. Momose, A. Phase-sensitive imaging and phase tomography using X-ray interferometers. *Opt. Exp.* **11**, 2303–2314. https://doi.org/10.1364/OE.11.002303 (2003).
19. Pfeiffer, F. *et al.* Hard-X-ray dark-field imaging using a grating interferometer. *Nat. Mater.* **7**, 134–137. https://doi.org/10.1038/nmat2096 (2008).
20. Weitkamp, T. *et al.* X-ray phase imaging with a grating interferometer. *Opt. Exp.* **13**, 6296–6304. https://doi.org/10.1364/OPEX.13.006296 (2005).
21. Berujon, S., Wang, H. & Sawhney, K. X-ray multimodal imaging using a random-phase object. *Phys. Rev. A* **86**(6), 063813. https://doi.org/10.1103/PhysRevA.86.063813 (2012).
22. Morgan, K. S., Paganin, D. M. & Siu, K. K. W. Quantitative single-exposure X-ray phase contrast imaging using a single attenuation grid. *Opt. Exp.* **19**, 19781–19789 (2011).
23. Pfeiffer, F., Weitkamp, T., Bunk, O. & David, C. Phase retrieval and differential phase-contrast imaging with low-brilliance X-ray sources. *Nat. Phys.*[SPACE]https://doi.org/10.1038/nphys265 (2006).
24. Takeda, M., Ina, H. & Kobayashi, S. Fourier-transform method of fringe-pattern analysis for computer-based topography and interferometry. *J. Opt. Soc. Am.* **72**, 156–160. https://doi.org/10.1364/JOSA.72.000156 (1982).
25. David, C. *et al.* Fabrication of diffraction gratings for hard X-ray phase contrast imaging. *Microelectron. Eng.* **84**, 1172–1177. https://doi.org/10.1016/j.mee.2007.01.151 (2007) (proceedings of the 32nd international conference on micro- and nano-engineering).
26. Willner, M. *et al.* Quantitative X-ray phase-contrast computed tomography at 82 keV. *Opt. Exp.* **21**, 4155–4166. https://doi.org/10.1364/OE.21.004155 (2013).
27. Sarapata, A. *et al.* Quantitative imaging using high-energy X-ray phase-contrast CT with a 70 kvp polychromatic X-ray spectrum. *Opt. Exp.* **23**, 523–535. https://doi.org/10.1364/OE.23.000523 (2015).
28. Braig, E. *et al.* Direct quantitative material decomposition employing grating-based X-ray phase-contrast CT. *Sci. Rep.* **8**, 16394. https://doi.org/10.1038/s41598-018-34809-6 (2018).
29. Gresil, M. *et al.* EVITA Project: Comparison between traditional non-destructive techniques and phase contrast X-ray imaging applied to aerospace carbon fibre reinforced polymer. *Appl. Compos. Mater.* **24**, 513–524. https://doi.org/10.1007/s10443-016-9540-1 (2017).
30. Senck, S. *et al.* Microcrack characterization in loaded CFRP laminates using quantitative two- and three-dimensional X-ray dark-field imaging. *Compos. Part A Appl. Sci. Manuf.* **115**, 206–214. https://doi.org/10.1016/j.compositesa.2018.09.023 (2018).
31. Glinz, J. *et al.* A comparison of X-ray attenuation, differential phase, and dark-field contrast imaging for the detection of porosity in carbon fiber reinforced cyanate ester. *NDT & E Int.* **147**, 103194. https://doi.org/10.1016/j.ndteint.2024.103194 (2024).
32. Shoukroun, D. *et al.* Enhanced composite plate impact damage detection and characterisation using X-ray refraction and scattering contrast combined with ultrasonic imaging. *Compos. Part B Eng.* **181**, 107579. https://doi.org/10.1016/j.compositesb.2019.107579 (2020).
33. Primot, J. Three-wave lateral shearing interferometer. *Appl. Opt.* **32**, 6242–6249. https://doi.org/10.1364/AO.32.006242 (1993).
34. Rizzi, J. *et al.* X-ray phase contrast imaging and noise evaluation using a single phase grating interferometer. *Opt. Exp.* **21**, 17340–17351. https://doi.org/10.1364/OE.21.017340 (2013).
35. Giakoumakis, G., Stolidi, A. & Primot, J. High resolution X-ray phase contrast imaging for non-destructive testing of composite materials. *ReJNDT* (special issue 'Frontiers in Nondestructive Testing and Evaluation: Academic Insights) (2022/23). https://doi.org/10.58286/29364 (2024).
36. Giakoumakis, G., Primot, J., Jarnac, A., Guitard, L. & Stolidi, A. Artifacts reduction in high-acutance phase images for X-ray grating interferometry. *Opt. Exp.* **30**, 41147–41156 (2022).

37. Stolidi, A., Giakoumakis, G., Primot, J., Jarnac, A. & Tisseur, D. Confidence map tool for gradient-based X-ray phase contrast imaging. *Opt. Exp.* **30**, 4302–4311. https://doi.org/10.1364/OE.438876 (2022).
38. Berger, M. et al. Xcom: Photon cross sections database (version 1.5). https://doi.org/10.18434/T48G6X (Natl. Inst. Standards Technol., 2010).
39. Kirchdoerfer, T., Liebscher, A. & Ortiz, M. Cth shock physics simulation of non-linear material effects within an aerospace CFRP fastener assembly due to direct lightning attachment. *Compos. Struct.* **189**, 357–365. https://doi.org/10.1016/j.compstruct.2017.11.061 (2018).
40. AE-2 Lightning Committee. *Aircraft Lightning Environment and Related Test Waveforms*, (2013) https://doi.org/10.4271/ARP5412B.
41. Sousa Martins, R., Chemartin, L., Zaepffel, C., Lalande, P. & Soufiani, A. Electrical and hydrodynamic characterization of a high current pulsed arc. *J. Phys. D Appl. Phys.* **49**, 185204. https://doi.org/10.1088/0022-3727/49/18/185204 (2016).
42. Kapur, J. N., Sahoo, P. K. & Wong, A. K. A new method for gray-level picture thresholding using the entropy of the histogram. *Comput. Vis. Graph. Image Process.* **29**, 273–285 (1985).
43. Feldkamp, L. A., Davis, L. C. & Kress, J. W. Practical cone-beam algorithm. *JOSA A* **1**, 612–619 (1984).

Acknowledgements

The authors wish to thank the French Civil Aviation Authority (DGAC), France Relance and NextGenerationEU for their financial supports. The authors thank the Department of Materials and Structures (DMAS) from ONERA for the availability of the CFRP-test pieces. This research is part of the project ANR-23-CE42-0002 funded by the Agence Nationale de la Recherche.

Author contributions

R.SM. and A.J. conducted the lightning strike experiment on the CFRP sample. L.G. and A.S. imaged the CFRP using laboratory bench techniques and then performed attenuation tomography. The analytical study was subsequently carried out by L.G. The manuscript was written by L.G., A.J. and A.S. All authors reviewed the manuscript.

Competing interest

The authors declare no competing interests.

Additional information

Correspondence and requests for materials should be addressed to A.J.

Reprints and permissions information is available at www.nature.com/reprints.

Publisher's note Springer Nature remains neutral with regard to jurisdictional claims in published maps and institutional affiliations.